

# Fluorescence optical diffusion tomography

Adam B. Milstein, Seungseok Oh, Kevin J. Webb, Charles A. Bouman, Quan Zhang, David A. Boas, and R. P. Millane

A nonlinear, Bayesian optimization scheme is presented for reconstructing fluorescent yield and lifetime, the absorption coefficient, and the diffusion coefficient in turbid media, such as biological tissue. The method utilizes measurements at both the excitation and the emission wavelengths to reconstruct all unknown parameters. The effectiveness of the reconstruction algorithm is demonstrated by simulation and by application to experimental data from a tissue phantom containing the fluorescent agent Indocyanine Green. © 2003 Optical Society of America

OCIS codes: 170.6280, 290.7050, 100.3190, 100.6950, 170.3010, 290.3200.

## 1. Introduction

Optical diffusion tomography (ODT) is emerging as a powerful tissue imaging modality.<sup>1,2</sup> In ODT, images are comprised of the spatially dependent absorption and scattering properties of the tissue. Boundary measurements from several sources and detectors are used to recover the unknown parameters from a scattering model described by a partial differential equation. Contrast between the properties of diseased and healthy tissue might then be used in clinical diagnosis. In principle, sinusoidally modulated, continuous-wave (cw), or pulsed excitation light is launched into the biological tissue, where it undergoes multiple scattering and absorption before exiting. One can use the measured intensity and phase (or delay) information to reconstruct three-dimensional (3-D) maps of the absorption and scattering properties by optimizing a fit to diffusion model computations. As a result of the nonlinear dependence of the diffusion equation photon flux on the unknown parameters and the inherently 3-D nature of photon scattering, this inverse problem is

computationally intensive and must be solved iteratively.

A relatively modest intrinsic contrast between the optical parameters of diseased and healthy breast tissue has been reported in some studies.<sup>3,4</sup> Use of exogenous fluorescent agents has the potential to improve the contrast and thus to facilitate early diagnosis. In recent years, use of fluorescent indicators as exogenous contrast agents for *in vivo* imaging of tumors with near-infrared or visible light has shown great promise, attracting considerable interest.<sup>5-14</sup> In experimental studies with animal subjects,<sup>5-7,9,10,13,14</sup> fluorescence has been successfully used to visualize cancerous tissue *in vivo* near the skin surface. In addition, Ntziachristos *et al.*<sup>12</sup> have used ODT after Indocyanine Green (ICG) injection to image the absorption of a malignant breast tumor in a human subject. The injected fluorophore may preferentially accumulate in diseased tissue because of increased blood flow from tumor neovascularization.<sup>9</sup> Alternatively, the agent may have different decay properties in diseased tissue, which could be useful to localize tumors independently of fluorophore concentration.<sup>7</sup> In addition, contrast between tumors and surrounding tissue may be substantially improved by use of diagnostic agents that selectively target receptors specific to cancer cells.<sup>8,10,13,14</sup>

In frequency-domain fluorescence ODT, sinusoidally modulated light at the fluorophore's excitation wavelength is launched into the tissue. The excited fluorophore, when it decays to the ground state, emits light at a longer (emission) wavelength, and this emission is measured by an array of detection devices. These emission data are then used to perform a volumetric reconstruction of the yield (a measure of the fluorescence efficiency) and the lifetime (the flu-

---

A. B. Milstein, S. Oh, K. J. Webb (webb@ecn.purdue.edu), and C. A. Bouman are with the School of Electrical and Computer Engineering, Purdue University, West Lafayette, Indiana 47907-1285. Q. Zhang and D. A. Boas are with the Nuclear Magnetic Resonance Center, Massachusetts General Hospital, Harvard Medical School, Charlestown, Massachusetts 02129. R. P. Millane is with the Department of Electrical and Computer Engineering, University of Canterbury, Christchurch, New Zealand.

Received 31 August 2002; revised manuscript received 19 December 2002.

0003-6935/03/163081-14\$15.00/0

© 2003 Optical Society of America

orescent decay parameter). However, the multiple scattering in tissue complicates the reconstruction.<sup>15,16</sup> The emission intensity of the fluorophore is proportional to the optical intensity at the excitation wavelength at that position, which depends in turn on the optical parameters of the scattering domain at the excitation wavelength. Therefore a rigorous reconstruction of fluorescence property maps should also include reconstructions of absorption and scattering parameters at the excitation and emission wavelengths. In addition, reconstruction of the unknown absorption and scattering coefficients by use of ODT can function as an adjunct image to the fluorescence image in screening for tumors.

Fluorescence imaging simulations with 3-D (Ref. 17) and two-dimensional<sup>18–20</sup> geometries have reconstructed fluorescence yield and lifetime parameters. These simulations have generally assumed that the absorption and scattering parameters are known in advance, except for Roy and Sevick-Muraca<sup>17</sup> who also reconstructed the excitation wavelength absorption. In an early experimental result, Chang *et al.*<sup>21</sup> used a transport theory model to reconstruct fluorescent yield in a heterogeneous tissue phantom containing Rhodamine 6G. Their study used cw data recorded in a two-dimensional plane geometry. Recently, Ntziachristos and Weissleder<sup>22</sup> used a normalized Born approximation to reconstruct 3-D fluorescent heterogeneities containing the near-infrared cyanine dye Cy5.5 embedded in a tissue phantom. Under the assumption of known background optical properties and absorbers limited to a perturbative regime, their technique can circumvent the need for recording background measurements before contrast agent administration.

The development of nonlinear inversion methods for ODT is necessary because of the fundamentally limited accuracy of methods that linearize the forward model.<sup>23</sup> Previously, we have presented a nonlinear Bayesian approach<sup>24–26</sup> and shown that it produces high-quality images compared with previous methods such as the distorted Born iterative method.<sup>27</sup> The method formulates the inversion as the optimization of an objective function that incorporates a model of the detection system and *a priori* knowledge about the image properties. We found that a neighborhood regularization scheme used in a Bayesian framework reduces artifacts characteristic of previous approaches that impose a penalty on the norm of the image updates.<sup>24</sup> The inversion can be made more computationally efficient by multigrid techniques.<sup>25</sup>

Here we extend our previous approach to include fluorescence yield and lifetime in the inverse problem. We present a new inversion algorithm and a measurement scheme for reconstructing all the unknown fluorescence, absorption, and diffusion parameters. Numerical simulations validate the scheme and demonstrate its computational efficacy. We use the method to image a spherical heterogeneity in a

tissue phantom by use of transmission data collected by a cw imaging device. The heterogeneity contains ICG, a fluorescent diagnostic agent approved by the U.S. Food and Drug Administration for use in the near-infrared range, where biomedical imaging with light is most practical.

## 2. Fluorescence Diffusion Tomography Problem

The transport of modulated light [at modulation angular frequency  $\omega$ , i.e.,  $\exp(j\omega t)$  variation] in a fluorescent, highly scattering medium with an external source at the excitation wavelength is modeled by use of the coupled diffusion equations<sup>15,16,28</sup>:

$$\nabla \cdot [D_x(\mathbf{r})\nabla\phi_x(\mathbf{r}, \omega)] - [\mu_{a_x}(\mathbf{r}) + j\omega/c]\phi_x(\mathbf{r}, \omega) = -\delta(\mathbf{r} - \mathbf{r}_{s_k}), \quad (1)$$

$$\nabla \cdot [D_m(\mathbf{r})\nabla\phi_m(\mathbf{r}, \omega)] - [\mu_{a_m}(\mathbf{r}) + j\omega/c]\phi_m(\mathbf{r}, \omega) = -\phi_x(\mathbf{r}, \omega)\eta\mu_{a_f}(\mathbf{r}) \frac{1 - j\omega\tau(\mathbf{r})}{1 + [\omega\tau(\mathbf{r})]^2}, \quad (2)$$

where the subscripts  $x$  and  $m$ , respectively, denote excitation and emission wavelengths  $\lambda_x$  and  $\lambda_m$ ;  $\phi(\mathbf{r}, \omega)$  is the complex modulation envelope of the photon flux;  $\delta(\mathbf{r})$  is the Dirac function; and  $\mathbf{r}_{s_k}$  is the location of the excitation point source. We also assume single exponential decay in this model. The optical parameters are the diffusion coefficients  $D(\mathbf{r})$  and the absorption coefficients  $\mu_a(\mathbf{r})$ . The fluorescence parameters are the lifetime  $\tau(\mathbf{r})$  and the fluorescent yield  $\eta\mu_{a_f}(\mathbf{r})$ . The fluorescent yield incorporates the fluorophore's quantum efficiency  $\eta$  (which depends on the type of fluorophore and the chemical environment) and its absorption coefficient  $\mu_{a_f}$  (which depends on the fluorophore concentration). Note the right-hand side of Eq. (2), where the light absorbed by fluorophores and subsequently emitted at the emission wavelength is incorporated into an effective source term. In the case of an external point source at the emission wavelength, the flux is governed by

$$\nabla \cdot [D_m(\mathbf{r})\nabla\phi_m(\mathbf{r}, \omega)] - [\mu_{a_m}(\mathbf{r}) + j\omega/c]\phi_m(\mathbf{r}, \omega) = -\delta(\mathbf{r} - \mathbf{r}_{s_k}). \quad (3)$$

In the most general case, the unknown parameters in Eqs. (1) and (2) are  $\mu_{a_x}$ ,  $\mu_{a_m}$ ,  $D_x$ ,  $D_m$ ,  $\tau$ , and  $\eta\mu_{a_f}$ . Reconstructions of the  $D_x$  and  $\mu_{a_x}$  images can be obtained by use of data from sources and detectors at the excitation wavelength  $\lambda_x$ . Similarly,  $D_m$  and  $\mu_{a_m}$  can be obtained by use of data from sources and detectors at the emission wavelength  $\lambda_m$ . Finally, having found these parameters, use of sources at  $\lambda_x$  and detectors filtered at  $\lambda_m$  will yield the fluorescence parameters. Figure 1 depicts this measurement approach schematically.

After discretizing the domain into  $N$  voxels of equal size, one can regard the unknown parameters as

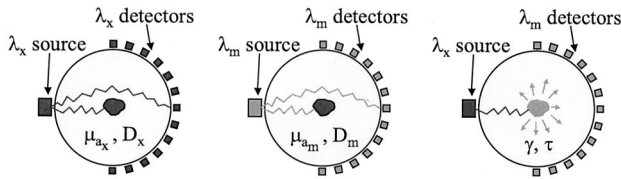


Fig. 1. Proposed measurement scheme.

three image vectors, each corresponding to a measurement set. Let  $\mathbf{r}_i$  denote the position of the  $i$ th voxel centroid, i.e., the location of a node in a Cartesian finite-difference representation of Eqs. (1)–(3). We define the image vectors as

$$\begin{aligned} \mathbf{x}_x &= \begin{bmatrix} \mathbf{x}_{xa} \\ \mathbf{x}_{xb} \end{bmatrix} = [\mu_{a_x}(\mathbf{r}_1) \cdots \mu_{a_x}(\mathbf{r}_N), D_x(\mathbf{r}_1) \cdots D_x(\mathbf{r}_N)]^T, \\ \mathbf{x}_m &= \begin{bmatrix} \mathbf{x}_{ma} \\ \mathbf{x}_{mb} \end{bmatrix} = [\mu_{a_m}(\mathbf{r}_1) \cdots \mu_{a_m}(\mathbf{r}_N), D_m(\mathbf{r}_1) \cdots D_m(\mathbf{r}_N)]^T, \\ \mathbf{x}_f &= \begin{bmatrix} \mathbf{x}_{fa} \\ \mathbf{x}_{fb} \end{bmatrix} = [\gamma(\mathbf{r}_1) \cdots \gamma(\mathbf{r}_N), \tau(\mathbf{r}_1) \cdots \tau(\mathbf{r}_N)]^T, \end{aligned} \quad (4)$$

where the subscript  $f$  denotes the fluorescence image and the superscript  $T$  denotes the transpose operation. Note that the three image vectors are each of size  $2N$ , consisting of two unknown parameter vectors of size  $N$ . In addition, we reparameterize the fluorescence unknowns  $\{\eta\mu_{a_f}, \tau\}$  to  $\{\gamma, \tau\}$  using

$$\gamma(\mathbf{r}, \omega) = \eta\mu_{a_f}(\mathbf{r}) \frac{1}{1 + [\omega\tau(\mathbf{r})]^2}, \quad (5)$$

which, when substituted into Eq. (2), yields

$$\begin{aligned} \nabla \cdot [D_m(\mathbf{r})\nabla\phi_m(\mathbf{r}, \omega)] - [\mu_{a_m}(\mathbf{r}) + j\omega/c]\phi_m(\mathbf{r}, \omega) \\ = -\phi_x(\mathbf{r}, \omega)\gamma(\mathbf{r}, \omega)[1 - j\omega\tau(\mathbf{r})]. \end{aligned} \quad (6)$$

As explained in Appendix A, this new parameterization is useful because, in a sequential optimization scheme, it takes advantage of the inherent linearity of the fluorescence inverse problem while allowing regularization to be applied to  $\tau$  directly. The sets of flux measurements corresponding to the above image vectors are defined, respectively, as  $\mathbf{y}_x$ ,  $\mathbf{y}_m$ , and  $\mathbf{y}_f$ .

### 3. Inversion

The estimation of each of the unknown images  $\{\mathbf{x}_x, \mathbf{x}_m, \mathbf{x}_f\}$  from the corresponding observations  $\{\mathbf{y}_x, \mathbf{y}_m, \mathbf{y}_f\}$  is an ill-posed, typically underdetermined, inverse problem. As in previous studies,<sup>24–26,29</sup> we address this by formulating the inverse problem in a Bayesian framework. This framework allows the incorporation of *a priori* information, and it encapsulates all available information about the problem model into an objective function to be optimized. Let  $\mathbf{x}$  denote one of the images of Eqs. (4) and let  $\mathbf{y}$  denote its corresponding observations. We use Bayes' rule to

compute the maximum *a posteriori* (MAP) estimate, given by

$$\hat{\mathbf{x}}_{\text{MAP}} = \arg \max_{\mathbf{x} \geq 0} [p(\mathbf{y}|\mathbf{x}) + p(\mathbf{x})], \quad (7)$$

where  $p(\mathbf{y}|\mathbf{x})$  is the data likelihood and  $p(\mathbf{x})$  is the prior density for the image. The data likelihood can be formed from a Gaussian model when we consider, for example, the physical properties of a photocurrent shot-noise-limited measurement system.<sup>24</sup> This gives

$$p(\mathbf{y}|\mathbf{x}) = \frac{1}{(\pi\alpha)^P |\Lambda|^{-1}} \exp\left[-\frac{\|\mathbf{y} - \mathbf{f}(\mathbf{x})\|_{\Lambda}^2}{\alpha}\right], \quad (8)$$

where  $P$  is the number of measurements;  $\mathbf{f}$  is the appropriate forward operator;  $\alpha$  is a scalar parameter that scales the noise variance; and, for an arbitrary vector  $\mathbf{w}$ ,  $\|\mathbf{w}\|_{\Lambda}^2 = \mathbf{w}^H \Lambda \mathbf{w}$  (where  $H$  denotes Hermitian transpose) and  $(\alpha/2)\Lambda^{-1}$  is the covariance matrix. In a small signal shot-noise model, the measurements are independent and normally distributed with a mean equal to the exact (noiseless) measurement and a variance proportional to the exact measurement at a modulation frequency of zero (dc). Following Ye *et al.*,<sup>24</sup> we approximate the dc flux for the  $i$ th datum as  $|y_i|$ . The resulting covariance matrix is given by

$$\frac{\alpha}{2} \Lambda^{-1} = \frac{\alpha}{2} \text{diag}(|y_1|, |y_2|, \dots, |y_P|). \quad (9)$$

For the prior density  $p(\mathbf{x})$ , we use the generalized Gaussian Markov random field (GGMRF) model, which enforces smoothness in the solution while preserving sharp edge transitions.<sup>24,30</sup> For each node (representing a voxel) inside the image, we form a 3-D neighborhood from the 26 adjacent nodes. Let  $\mathbf{x}^T = [\mathbf{x}_a^T, \mathbf{x}_b^T]$ , as in Eqs. (4). Assuming independence of  $\mathbf{x}_a$  and  $\mathbf{x}_b$ , the density function is given by

$$\begin{aligned} p(\mathbf{x}) &= p(\mathbf{x}_a) \cdot p(\mathbf{x}_b) \quad (10) \\ &= \left[ \frac{1}{\sigma_a^N z(p_a)} \exp\left(-\frac{1}{p_a \sigma_a^{p_a}} \right. \right. \\ &\quad \times \left. \left. \sum_{\{i,j\} \in \mathcal{N}_a} b_{i-j} |x_i - x_j|^{p_a} \right) \right] \\ &\quad \times \left[ \frac{1}{\sigma_b^N z(p_b)} \exp\left(-\frac{1}{p_b \sigma_b^{p_b}} \right. \right. \\ &\quad \times \left. \left. \sum_{\{i,j\} \in \mathcal{N}_b} b_{i-j} |x_i - x_j|^{p_b} \right) \right], \end{aligned} \quad (11)$$

where the subscripts  $a$  and  $b$  have the same meaning as in Eqs. (4),  $x_i$  denotes the  $i$ th node of  $\mathbf{x}$ , the set  $\mathcal{N}$  consists of all pairs of neighboring nodes, and  $b_{i-j}$  is the weighting coefficient corresponding to the  $i$ th and  $j$ th nodes. The coefficients  $b_{i-j}$  are assigned to be inversely proportional to the node separation in a

cube-shaped node layout, with the requirement that that  $\sum_j b_{i-j} = 1$ . The constants  $p$  and  $\sigma$  control the

Eq. (7) than the  $\hat{\alpha}$  updates. For each image, we form an objective function from Eqs. (8) and (11):

$$c(\mathbf{x}_x, \hat{\alpha}_x) = \frac{1}{\hat{\alpha}_x} \|\mathbf{y}_x - \mathbf{f}_x(\mathbf{x}_x)\|_{\Lambda_x}^2 + \frac{1}{p_{xa}\sigma_{xa}^{p_{xa}}} \sum_{\{i,j\} \in \mathcal{N}_{xa}} b_{i-j} |x_{xa_i} - x_{xa_j}|^{p_{xa}} + \frac{1}{p_{xb}\sigma_{xb}^{p_{xb}}} \sum_{\{i,j\} \in \mathcal{N}_{xb}} b_{i-j} |x_{xb_i} - x_{xb_j}|^{p_{xb}}, \quad (18)$$

$$c(\mathbf{x}_m, \hat{\alpha}_m) = \frac{1}{\hat{\alpha}_m} \|\mathbf{y}_m - \mathbf{f}_m(\mathbf{x}_m)\|_{\Lambda_m}^2 + \frac{1}{p_{ma}\sigma_{ma}^{p_{ma}}} \sum_{\{i,j\} \in \mathcal{N}_{ma}} b_{i-j} |x_{ma_i} - x_{ma_j}|^{p_{ma}} + \frac{1}{p_{mb}\sigma_{mb}^{p_{mb}}} \sum_{\{i,j\} \in \mathcal{N}_{mb}} b_{i-j} |x_{mb_i} - x_{mb_j}|^{p_{mb}}, \quad (19)$$

$$c(\mathbf{x}_f, \hat{\mathbf{x}}_x, \hat{\mathbf{x}}_m, \hat{\alpha}_f) = \frac{1}{\hat{\alpha}_f} \|\mathbf{y}_f - \mathbf{f}_f(\mathbf{x}_f, \hat{\mathbf{x}}_x, \hat{\mathbf{x}}_m)\|_{\Lambda_f}^2 + \frac{1}{p_{fa}\sigma_{fa}^{p_{fa}}} \sum_{\{i,j\} \in \mathcal{N}_{fa}} b_{i-j} |x_{fa_i} - x_{fa_j}|^{p_{fa}} + \frac{1}{p_{fb}\sigma_{fb}^{p_{fb}}} \sum_{\{i,j\} \in \mathcal{N}_{fb}} b_{i-j} |x_{fb_i} - x_{fb_j}|^{p_{fb}}. \quad (20)$$

shape and scale of the distribution, and the factor  $z(p)$  is a normalization term.

As in previous research,<sup>25</sup> we incorporate  $\alpha$  into the inverse problem as an unknown for each image. We found that this tends to improve the robustness and speed of convergence. As a result, we perform a joint maximum *a posteriori* estimation of both  $\mathbf{x}$  and  $\alpha$  for each image:

$$\hat{\mathbf{x}}_x = \arg \max_{\mathbf{x}_x \geq 0, \alpha_x} [p(\mathbf{x}_x | \mathbf{y}_x, \alpha_x)], \quad (12)$$

$$\hat{\mathbf{x}}_m = \arg \max_{\mathbf{x}_m \geq 0, \alpha_m} [p(\mathbf{x}_m | \mathbf{y}_m, \alpha_m)], \quad (13)$$

$$\hat{\mathbf{x}}_f = \arg \max_{\mathbf{x}_f \geq 0, \alpha_f} [p(\mathbf{x}_f | \mathbf{y}_f, \alpha_f, \hat{\mathbf{x}}_x, \hat{\mathbf{x}}_m)]. \quad (14)$$

The estimations of  $\mathbf{x}_x$  and  $\mathbf{x}_m$  are performed independently of each other, with Eqs. (1) and (3) used as the respective forward models. Subsequently, these estimates are incorporated into the coupled diffusion equations [Eqs. (1) and (2)] to estimate  $\mathbf{x}_f$ .

Let  $\mathbf{x}$  and  $\alpha$  correspond to one of the images in Eqs. (12)–(14). Ye *et al.*<sup>25</sup> showed that the above reconstructions are equivalent to one maximizing the log posterior probability  $l(\mathbf{x})$ , which can be derived with Eqs. (7), (8), and (11):

$$l(\mathbf{x}) = -P \ln \|\mathbf{y} - \mathbf{f}(\mathbf{x})\|_{\Lambda}^2 - \frac{1}{p_a \sigma_a^{p_a}} \sum_{\{i,j\} \in \mathcal{N}_a} b_{i-j} |x_i - x_j|^{p_a} - \frac{1}{p_b \sigma_b^{p_b}} \sum_{\{i,j\} \in \mathcal{N}_b} b_{i-j} |x_i - x_j|^{p_b}. \quad (15)$$

Optimizing  $l(\mathbf{x})$  can be implemented by alternating closed-form updates of  $\hat{\alpha}$  with updates of  $\hat{\mathbf{x}}$ <sup>25</sup>:

$$\hat{\alpha} = \frac{1}{P} \|\mathbf{y} - \mathbf{f}(\hat{\mathbf{x}})\|_{\Lambda}^2, \quad (16)$$

$$\hat{\mathbf{x}} \approx \arg \max_{\mathbf{x} \geq 0} [\ln p(\mathbf{y} | \mathbf{x}, \hat{\alpha}) + \ln p(\mathbf{x} | \hat{\alpha})], \quad (17)$$

where  $\approx$  implies an update iteration rather than a full optimization. The  $\hat{\mathbf{x}}$  updates represent more computationally expensive steps toward optimizing

The variables have the same meaning as in Eqs. (8) and (11), and their subscripts have the same meaning as in Eqs. (4). Note that forward operator  $\mathbf{f}_f$  is a function of  $\mathbf{x}_f$  and the estimates  $\hat{\mathbf{x}}_x$  and  $\hat{\mathbf{x}}_m$ . In principle, one could jointly optimize Eqs. (18)–(20) over  $\mathbf{x}_x$ ,  $\mathbf{x}_m$ , and  $\mathbf{x}_f$ , but for computational simplicity, we first optimize Eqs. (18) and (19) and subsequently incorporate the estimates into Eq. (20). With the objective functions defined by Eqs. (18)–(20) established, an optimization algorithm to minimize these costs is needed, which is described in Section 4.

#### 4. Iterative Coordinate Descent Optimization

The optimizations of Eqs. (18)–(20) are performed by use of the iterative coordinate descent (ICD) algorithm,<sup>24,26,31</sup> a sequential single-site update scheme similar to the Gauss–Seidel method used in other problems. One ICD scan consists of the formation of a local quadratic approximation to the cost function, followed by an update of each image element individually to minimize the approximate objective function. On each subsequent scan, the Fréchet derivative of the nonlinear forward operator is recomputed, and a new quadratic approximation is made.

Once again, let  $\mathbf{x}$  denote one of the three images to be optimized. During the scan, the individual voxels of  $\mathbf{x}$  are sequentially updated in random order. At the beginning of the scan,  $\mathbf{f}(\mathbf{x})$  is first expressed by use of a Taylor expansion as

$$\|\mathbf{y} - \mathbf{f}(\mathbf{x})\|_{\Lambda}^2 \approx \|\mathbf{y} - \mathbf{f}(\hat{\mathbf{x}}) - \mathbf{F}'(\hat{\mathbf{x}})\Delta\mathbf{x}\|_{\Lambda}^2, \quad (21)$$

where  $\Delta\mathbf{x} = \mathbf{x} - \hat{\mathbf{x}}$ , and  $\mathbf{F}'(\hat{\mathbf{x}})$  represents the Fréchet derivative of  $\mathbf{f}(\mathbf{x})$  with respect to  $\mathbf{x}$  at  $\mathbf{x} = \hat{\mathbf{x}}$ . Using Eq. (21), we formulate the approximate cost function:

$$c(\mathbf{x}, \hat{\alpha}) \approx \frac{1}{\hat{\alpha}} \|\mathbf{z} - \mathbf{F}'(\hat{\mathbf{x}})\mathbf{x}\|_{\Lambda}^2 + \frac{1}{p_a \sigma_a^{p_a}} \sum_{\{i,j\} \in \mathcal{N}_a} b_{i-j} |x_i - x_j|^{p_a} + \frac{1}{p_b \sigma_b^{p_b}} \sum_{\{i,j\} \in \mathcal{N}_b} b_{i-j} |x_i - x_j|^{p_b}, \quad (22)$$

where

$$\mathbf{z} = \mathbf{y} - \mathbf{f}(\hat{\mathbf{x}}) + \mathbf{F}'(\hat{\mathbf{x}})\hat{\mathbf{x}}. \quad (23)$$

With the other image elements fixed, the ICD update for  $\hat{x}_i$  is given by

$$\hat{x}_i = \arg \min_{x_i \geq 0} \left\{ \frac{1}{\hat{\alpha}} \|\mathbf{y} - \mathbf{f}(\hat{\mathbf{x}}) - [\mathbf{F}'(\hat{\mathbf{x}})]_{*(i)}(x_i - \hat{x}_i)\|_{\Lambda}^2 + \frac{1}{p\sigma^p} \sum_{j \in \mathcal{N}_i} b_{i-j} |x_i - \hat{x}_j|^p \right\}, \quad (24)$$

where  $[\mathbf{F}'(\hat{\mathbf{x}})]_{*(i)}$  is the  $i$ th column of the Fréchet derivative matrix and  $\mathcal{N}_i$  is the set of nodes neighboring node  $i$ , and  $p$  and  $\sigma$  are chosen appropriately from  $\{p_a, p_b\}$  and  $\{\sigma_a, \sigma_b\}$ . This one-dimensional minimization is solved by use of a simple half-interval search.<sup>24</sup> The Fréchet derivative matrices used for each image are given in Appendix A. In Appendix B we summarize the ICD optimization algorithm in pseudocode form.

Previously, we found that multiresolution techniques can reduce the computational burden and improve robustness of convergence for the ODT problem.<sup>25</sup> Hence, for large computational domains, it may be beneficial to perform several ICD scans at a reduced resolution followed by interpolation as an initialization step for the full-resolution problem.

## 5. Simulations

Figure 2 shows cross-sectional images of a  $17.3 \text{ cm} \times 17.3 \text{ cm} \times 6 \text{ cm}$  tissue phantom having background values  $\mu_{a,x,m} = 0.01 \text{ cm}^{-1}$ ,  $D_{x,m} = 0.047 \text{ cm}$ ,  $\tau = 0 \text{ ns}$ , and  $\eta\mu_{a_f} = 0 \text{ cm}^{-1}$ . A slightly off-center spherical heterogeneity with a diameter of roughly  $3 \text{ cm}$  is present, with  $\mu_{a_x} = 0.05 \text{ cm}^{-1}$ ,  $\mu_{a_m} = 0.01 \text{ cm}^{-1}$ ,  $D_x$  and  $D_m = 0.30 \text{ cm}$ ,  $\tau = 0.55 \text{ ns}$ , and  $\eta\mu_{a_f} = 0.02 \text{ cm}^{-1}$ . Figure 2(g) shows the location and size of the fluorophore as the  $\eta\mu_{a_f} = 0.01\text{-cm}^{-1}$  isosurface. As shown in Fig. 3, the bottom face of the domain contains 16 sources (modulated at  $70 \text{ MHz}$ ) arranged in a  $4 \times 4$  grid pattern. On the top face, 16 detectors are placed in an identical grid. Using multigrid finite differences<sup>32</sup> to solve the diffusion equations, we generated synthetic measurements. Additive noise was introduced by use of the approximate shot-noise model of Eqs. (8) and (9), giving an average signal-to-noise ratio of  $34 \text{ dB}$  and a maximum signal-to-noise ratio of  $41 \text{ dB}$ . In the forward solution, an extrapolated zero-flux boundary condition<sup>33</sup> was used to model the free-space absorbing boundaries.

For each of the  $\mathbf{x}_x$ ,  $\mathbf{x}_m$ , and  $\mathbf{x}_f$  inversions, 20 ICD iterations at a resolution of  $17 \times 17 \times 9$  nodes, followed by 20 ICD iterations at a resolution of  $33 \times 33 \times 17$  nodes, were performed. For the nonlinear  $\mathbf{x}_x$  and  $\mathbf{x}_m$  problems, multigrid finite differences were used to solve the forward model prior to each ICD image update. During the inversions, the log posterior probability was evaluated as the convergence criterion. For each image, convergence (with subsequent iterations changing the images very little) was obtained in approximately 10 min of computation on

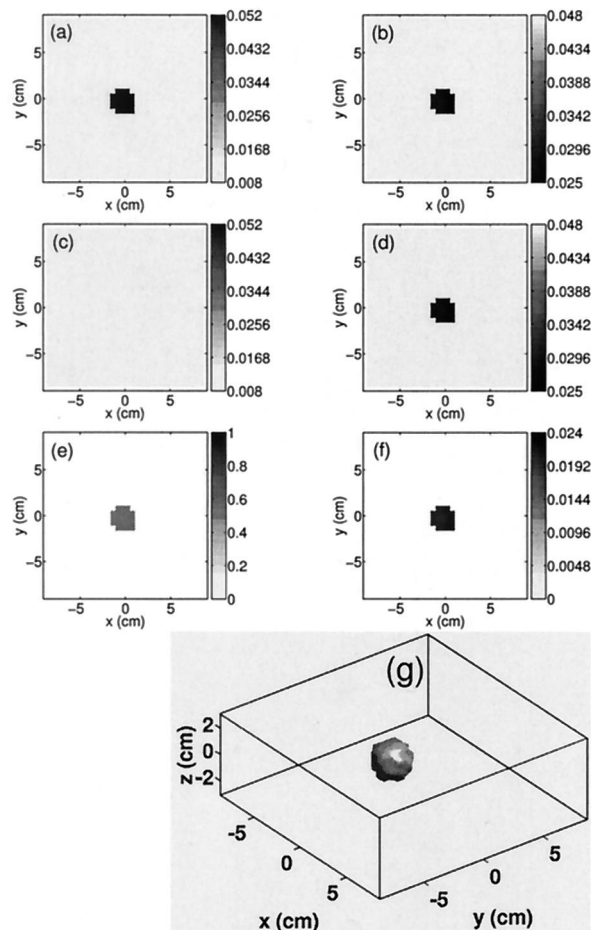


Fig. 2. True phantom, with cross sections of the widest part of the heterogeneity: (a)  $\mu_{a_x}$  is in  $\text{cm}^{-1}$ , (b)  $D_x$  is in  $\text{cm}$ , (c)  $\mu_{a_m}$  is in  $\text{cm}^{-1}$ , (d)  $D_m$  is in  $\text{cm}$ , (e)  $\tau$  is in  $\text{ns}$ , (f)  $\eta\mu_{a_f}$  is in  $\text{cm}^{-1}$ , (g)  $\eta\mu_{a_f} = 0.01 \text{ cm}^{-1}$  isosurface.

an AMD Athlon 1333-MHz workstation. Although automatic estimation of the GGMRF hyperparameters  $p$  and  $\sigma$  is in principle possible with a maximum-likelihood estimation technique,<sup>34</sup> we follow Ye *et al.*<sup>24</sup> and use parameter values that empirically give good results. For each reconstruction, the

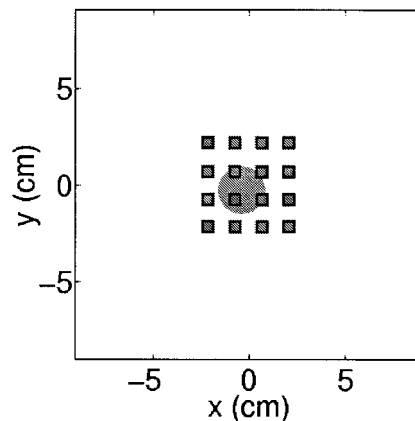


Fig. 3. Grid used for both sources and detectors in the simulation, with the relative location of the sphere depicted.

estimates were initialized with homogeneous images equal to the correct background values, as the ICD method's convergence is slow for low-spatial-frequency image components.<sup>31</sup> We have shown previously that multigrid inversion methods in conjunction with ICD updates alleviate this difficulty,<sup>25,35,36</sup> but, again, we do not address them in this investigation.

Reconstructions  $\hat{\mu}_{a_x,m}$ ,  $\hat{D}_{x,m}$ ,  $\hat{\tau}$ , and  $\eta\hat{\mu}_{a_f}$  are shown in Fig. 4. We used  $p = 2.0$  in all the reconstructions and  $\sigma$  values of  $0.015 \text{ cm}^{-1}$ ,  $0.02 \text{ cm}$ ,  $0.5 \text{ ns}$ , and  $0.002 \text{ cm}^{-1}$  in computing  $\hat{\mu}_a$ ,  $\hat{D}$ ,  $\hat{\tau}$ , and  $\hat{\gamma}$ , respectively. The reconstructions are qualitatively and quantitatively accurate.

We conjecture that changes in the lifetime parameter  $\tau$  can be useful to distinguish between diseased and healthy tissue environments. Hence it is useful to determine if such changes are within the accuracy of the reconstruction algorithm. The simulation was repeated for four fluorophores, each with a different value of  $\tau$ :  $0.1375$ ,  $0.275$ ,  $0.55$ , and  $1.10 \text{ ns}$ . The procedure outlined above was performed for each image. To determine a single lifetime value for each reconstructed image, we used a weighted average:

$$\hat{\tau}_{\text{avg}} = \frac{\sum_{i=0}^{N-1} \hat{\gamma}(\mathbf{r}_i) \hat{\tau}(\mathbf{r}_i)}{\sum_{i=0}^{N-1} \hat{\gamma}(\mathbf{r}_i)}. \quad (25)$$

The weighted average is reasonable, as the reconstruction  $\hat{\tau}(\mathbf{r})$  could be significant in spurious regions where  $\eta\hat{\mu}_{a_f} \approx 0$ . It is also similar to the weighting that occurs in the source term of Eq. (6), which represents the effect of  $\tau$  on the data. Figure 5 shows a plot of  $\hat{\tau}_{\text{avg}}$  as a function of the true value. The result suggests that the method can track even small changes in diagnostic lifetime imaging applications.

We also investigated the propagation of error from the  $\hat{\mathbf{x}}_x$  and  $\hat{\mathbf{x}}_m$  images into the  $\hat{\mathbf{x}}_f$  result. We created a series of incorrect images for  $\hat{\mathbf{x}}_x$  and  $\hat{\mathbf{x}}_m$ , and we used the incorrect guesses in reconstructing  $\hat{\mathbf{x}}_f$ . The incorrect  $\hat{\mathbf{x}}_x$  and  $\hat{\mathbf{x}}_m$  images were homogeneous. We tested the effect of varying  $\mu_{a_x}$ ,  $D_x$ ,  $\mu_{a_m}$ , and  $D_m$ , and we computed an error metric to quantify the change. For the  $\eta\hat{\mu}_{a_f}$  results, the error metric was the normalized root-mean-squared error (NRMSE), defined as

$$\text{NRMSE} = \left[ \frac{\sum_{i=0}^{N-1} |\eta\hat{\mu}_{a_f}(\mathbf{r}_i) - \eta\mu_{a_f}(\mathbf{r}_i)|^2}{\sum_{i=0}^{N-1} |\eta\mu_{a_f}(\mathbf{r}_i)|^2} \right]^{1/2}. \quad (26)$$

For the  $\hat{\tau}$  results, the NRMSE is less appropriate, as  $\hat{\tau}$  may be nonzero in areas where  $\eta\hat{\mu}_{a_f} \approx 0$ . Hence, the error metric for  $\hat{\tau}$  was the fractional error,  $|\hat{\tau}_{\text{avg}} - \tau_{\text{true}}|/\tau_{\text{true}}$ . The plots in Figs. 6(a)–6(d) show the NRMSE for  $\eta\hat{\mu}_{a_f}$  as a function of background  $\mu_{a_x}$ ,  $D_x$ ,  $\mu_{a_m}$ , and  $D_m$ , respectively. The plots in Figs. 7(a)–7(d) show the fractional error for  $\hat{\tau}_{\text{avg}}$ , also as a function of background  $\mu_{a_x}$ ,  $D_x$ ,  $\mu_{a_m}$ , and  $D_m$ , respectively.

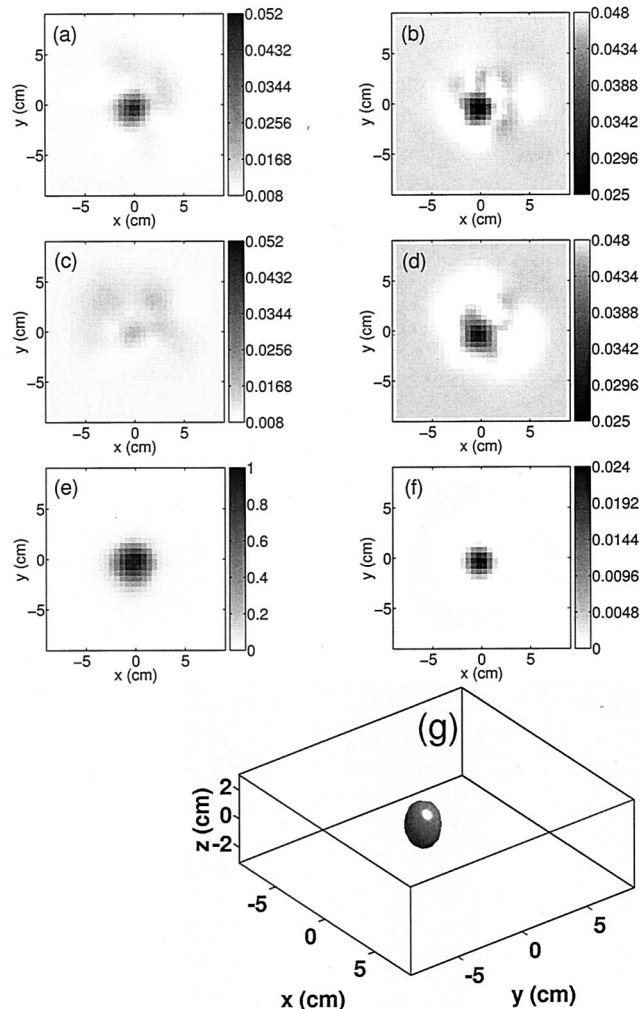


Fig. 4. Reconstructed phantom: (a)  $\hat{\mu}_{a_x}$  is in  $\text{cm}^{-1}$ , (b)  $\hat{D}_x$  is in  $\text{cm}$ , (c)  $\hat{\mu}_{a_m}$  is in  $\text{cm}^{-1}$ , (d)  $\hat{D}_m$  is in  $\text{cm}$ , (e)  $\hat{\tau}$  is in  $\text{ns}$ , (f)  $\eta\hat{\mu}_{a_f}$  is in  $\text{cm}^{-1}$ , (g)  $\eta\hat{\mu}_{a_f} = 0.01 \text{ cm}^{-1}$  isosurface.

Whenever one parameter was varied, the others were all set to the correct image's background value. In all plots, the plus symbols depict the error metric values resulting from the erroneous images, and the cross symbols shows the error metric value resulting when the reconstructions  $\hat{\mathbf{x}}_x$  and  $\hat{\mathbf{x}}_m$  were computed in advance. For  $\eta\hat{\mu}_{a_f}$ , the NRMSE is above 0.5 in all

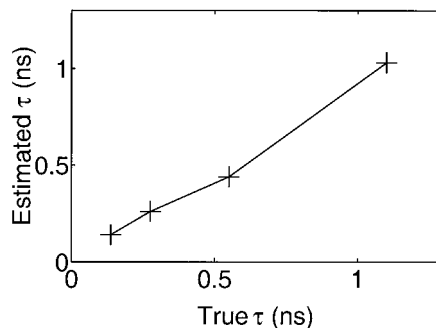


Fig. 5. Plot of estimate  $\hat{\tau}_{\text{avg}}$  versus the true value of  $\tau$ . The trend is almost linear, as desired.

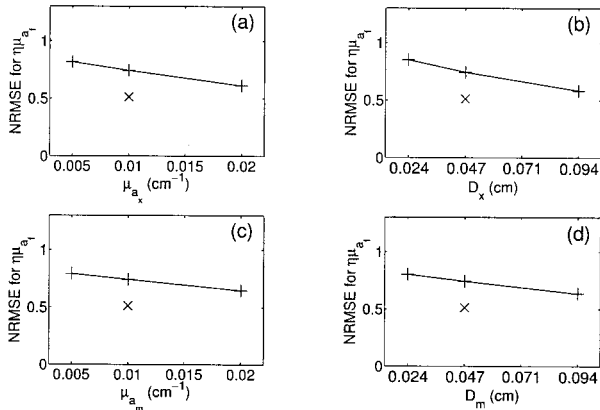


Fig. 6. NRMSE for  $\eta\hat{\mu}_{af}$  that is due to changes in assumed constant background values for (a)  $\mu_{ax}$  in  $\text{cm}^{-1}$ , (b)  $D_x$  in cm, (c)  $\mu_{am}$  in  $\text{cm}^{-1}$ , (d)  $D_m$  in cm. The + markers show results from assuming erroneous, constant images, whereas the  $\times$  markers show the results from computing  $\hat{\mathbf{x}}_x$  and  $\hat{\mathbf{x}}_m$  in advance.

cases, even when the full reconstruction was done. The increased NRMSE was likely due to blurring of the sharp edges as a result of our using the GGMRF prior model<sup>30</sup> with  $p = 2$ . Ignoring the heterogeneities, but using the correct background values, noticeably increased the NRMSE. However, the NRMSE changed relatively little over a range of incorrect background values for all the parameters  $\mu_{ax}$ ,  $D_x$ ,  $\mu_{am}$ , and  $D_m$ . The reconstructed  $\eta\hat{\mu}_{af}$  images also looked qualitatively similar. This suggests that the reconstructed yield was fairly robust to errors in  $\hat{\mathbf{x}}_x$  and  $\hat{\mathbf{x}}_m$ . However,  $\hat{\tau}$  was highly sensitive to use of the incorrect images.

## 6. Experimental Results

To further evaluate the proposed reconstruction method, we performed fluorescence measurements. We recorded the data using a cw imaging device and a versatile phantom box (shown in Fig. 8), both described in detail elsewhere.<sup>37</sup> In the absence of

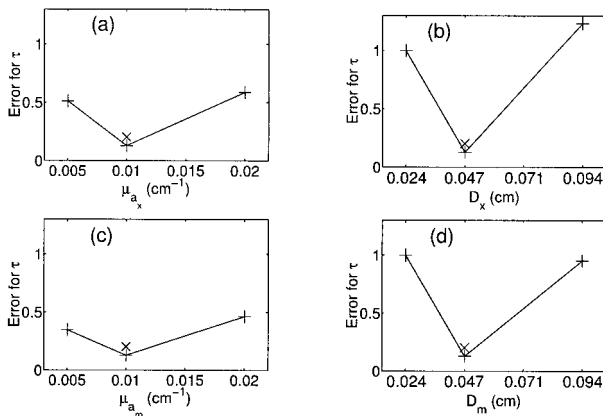


Fig. 7. Fractional error for  $\hat{\tau}_{\text{avg}}$  that is due to changes in assumed constant background values for (a)  $\mu_{ax}$  in  $\text{cm}^{-1}$ , (b)  $D_x$  in cm, (c)  $\mu_{am}$  in  $\text{cm}^{-1}$ , (d)  $D_m$  in cm. The + and  $\times$  markers have the same meaning as in Fig. 6.

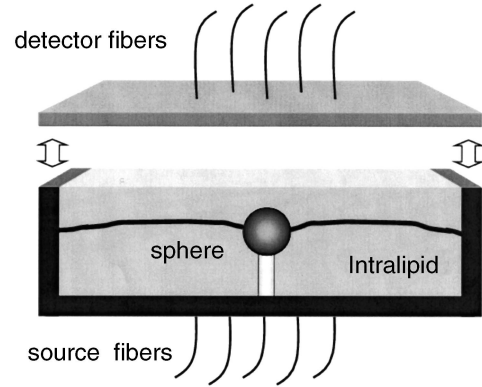


Fig. 8. Schematic of the phantom box showing the fibers, the spherical heterogeneity, and the removable lid.

phase information, we did not consider  $\tau$ , and we assumed  $D$  to be constant and known based on physical considerations. The instrument has laser diode sources available at both 690 and 830 nm, and it has avalanche photodiode detectors. Although 690-nm excitation is not ideal for ICG, a published excitation spectrum<sup>38</sup> indicates that the detected 830-nm emission intensity, with 690-nm excitation, is approximately 30% of the maximum value (obtained with 780-nm excitation), making it acceptable for this demonstration. The box had internal dimensions of  $16 \text{ cm} \times 16 \text{ cm} \times 3.8 \text{ cm}$ , where the last dimension is the vertical thickness. As shown in Fig. 9, nine source fibers were connected to the bottom plate (at  $z = -1.9 \text{ cm}$ ), and 14 detector fibers were connected to the top plate (at  $z = 1.9 \text{ cm}$ ). A hollow, surface-frosted-glass sphere with an outer diameter of 2 cm and a thickness of approximately 2 mm was mounted with its center near  $z = 0.7 \text{ cm}$ , as depicted in Fig. 10. This sphere was mounted on a small plastic stand on the bottom of the box. It was also connected to a closed circulation channel by thin, translucent rubber tubes leading outside the box, allowing the fluorophore solution to be titrated into the sphere from an external reservoir over the course of the experiment. The titration allowed comparable data to be taken both without and with the fluorophore present for analysis and calibration purposes.

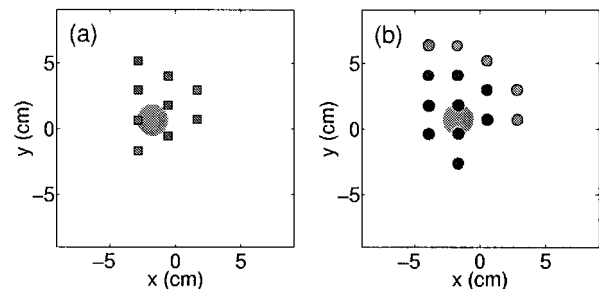


Fig. 9. Source and detector layout for the experiment. The darker circles represent the detector positions used in fluorescence measurements. The relative location of the sphere is also shown. (a) Bottom plate (sources). (b) Top plate (detectors).

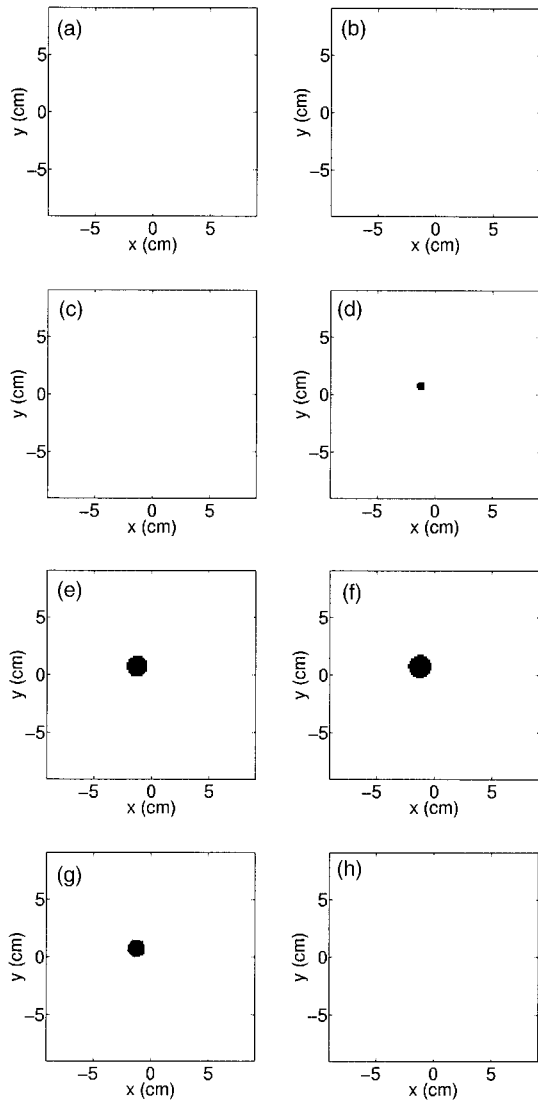


Fig. 10. True fluorophore location.  $z =$  (a)  $-1.82$ , (b)  $-1.30$ , (c)  $-0.78$ , (d)  $-0.26$ , (e)  $0.26$ , (f)  $0.78$ , (g)  $1.30$ , (h)  $1.82$  cm.

The box was filled with a suspension of 0.4% Intralipid. Assuming 690-nm excitation and 830-nm emission, this results in background values of approximately  $D_x = 0.071$  cm,  $D_m = 0.082$  cm,  $\mu_{a_x} = 0.0052$  cm $^{-1}$ , and  $\mu_{a_m} = 0.03$  cm $^{-1}$ .<sup>39,40</sup> The sphere was initially filled with the same suspension, creating an essentially homogeneous domain (apart from the glass sphere, rubber tubes, and plastic stand). Before administration of the ICG, we recorded two sets of measurements,  $\mathbf{y}_x^{(\text{base})}$  and  $\mathbf{y}_m^{(\text{base})}$ , using sources at 690 and 830 nm, respectively. We refer to the measurements recorded before ICG administration as baseline measurements. Subsequently, ICG was introduced into the sphere at a concentration of 1.0  $\mu\text{mol/l}$ . For the purposes of reconstructing  $\mu_{a_x}$ , we recorded the measurements, which we define as  $\mathbf{y}_x^{(\text{uncal})}$ , using 690-nm sources with no optical bandpass filters installed over the detectors. We neglect the fluorescence signal in these measurements, as

published quantum efficiency values<sup>16,41</sup> imply that its effect on the data is 2 or 3 orders of magnitude below the effects that are due to absorption. Following a similar procedure, 830-nm data, which we call  $\mathbf{y}_m^{(\text{uncal})}$ , were recorded (with no filters) to reconstruct  $\mu_{a_m}$ . Upon completion of these measurements, 830-nm bandpass filters with 12 nm FWHM (Newport 10LF10-830) were installed in front of the detectors to perform the fluorescence measurements. Because of a limited number of filters, only 9 of the 14 detectors were used to record the filtered fluorescence measurements (as shown in Fig. 9).

The installation of the filters required disconnection of the detector fibers from the detection devices. In principle, the disconnection and subsequent reconnection of the fibers could invalidate the previous baseline calibrations by potentially changing the detectors' coupling efficiencies. Such effects might adversely affect the  $\mathbf{y}_x$  and  $\mathbf{y}_m$  measurements. Hence a new baseline calibration procedure was performed. This need for multiple calibrations is a limitation in the design of the experiment that could be alleviated by use of a different detection scheme. For example, the instrument used by Ntziachristos and Weissleder,<sup>22</sup> in which a CCD camera imaged a detection fiber array, required the installation of only a single fluorescence filter without perturbing the detection fibers. Incorporating the unknown calibration parameters into the inverse problem<sup>29,42</sup> may also alleviate this difficulty.

To perform the new calibration, the ICG–Intralipid mixture was pumped out of the sphere and replaced with new Intralipid without ICG. Baseline measurements  $\mathbf{y}_f^{(\text{base})}$  with 690-nm sources and 830-nm detection were made. Subsequently, a new ICG–Intralipid mixture identical in concentration to the previous one was titrated into the sphere. With the ICG now present, we recorded fluorescence measurements  $\mathbf{y}_f^{(\text{uncal})}$  using 690-nm source excitation and 830-nm detection.

Before applying the reconstruction algorithm for  $\mathbf{x}_x$  and  $\mathbf{x}_m$ , we performed calibrations using the baseline data. Synthetic data  $\mathbf{y}_x^{(\text{comp})}$  (for 690-nm sources) and  $\mathbf{y}_m^{(\text{comp})}$  (for 830-nm sources) were computed for a homogeneous phantom with  $D_x = 0.071$  cm,  $D_m = 0.082$  cm,  $\mu_{a_x} = 0.0052$  cm $^{-1}$ , and  $\mu_{a_m} = 0.03$  cm $^{-1}$  on a  $33 \times 33 \times 17$  grid. We performed the calibrations by normalizing the following to the computed data:

$$y_{x_i} = y_{x_i}^{(\text{uncal})} \frac{y_{x_i}^{(\text{comp})}}{y_{x_i}^{(\text{base})}}, \quad (27)$$

$$y_{m_i} = y_{m_i}^{(\text{uncal})} \frac{y_{m_i}^{(\text{comp})}}{y_{m_i}^{(\text{base})}}, \quad (28)$$

where the subscript  $i$  represents the  $i$ th component of the data vector. This baseline calibration procedure estimates the unknown scaling and coupling efficiencies in the measurements. For the much dimmer fluorescence measurements, the baseline data  $\mathbf{y}_f^{(\text{base})}$  contained significant background signal. Calibra-

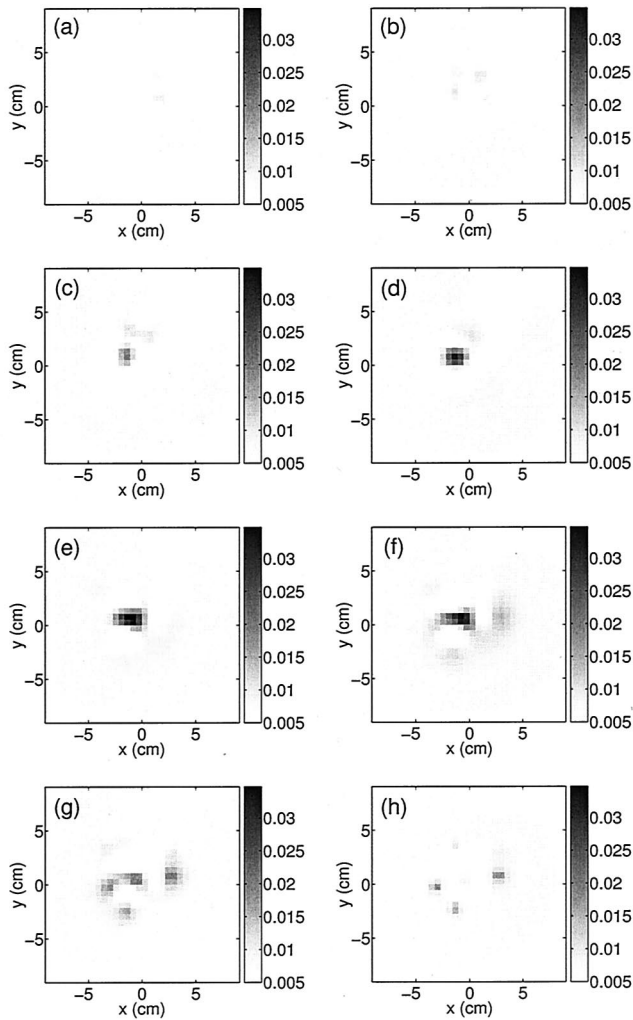


Fig. 11. Reconstructions of  $\mu_{ax}$  in  $\text{cm}^{-1}$ . Values of  $z$  for (a)–(h) are the same as in Fig. 10.

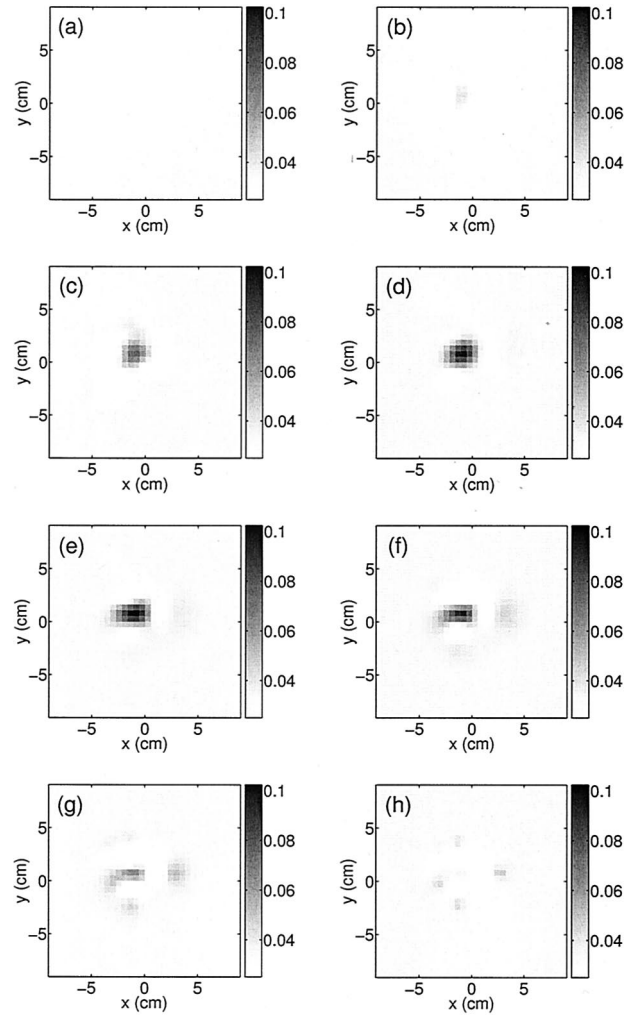


Fig. 12. Reconstructions of  $\mu_{am}$  in  $\text{cm}^{-1}$ . Values of  $z$  for (a)–(h) are the same as in Fig. 10.

tions were performed to account for the unknown coupling efficiencies and to remove these background components from the fluorescence data:

$$y_{fi} = [y_{fi}^{(\text{uncal})} - y_{fi}^{(\text{base})}] \frac{y_{xi}^{(\text{comp})}}{y_{xi}^{(\text{base})}}, \quad (29)$$

where we used the 690-nm calibration factors. The resulting fluorescence data contain an unknown scale factor that is due to the filter attenuation of the 830-nm fluorescence light.

The reconstructions  $\hat{\mu}_{ax}$  and  $\hat{\mu}_{am}$  are shown in Figs. 11 and 12, respectively. For each inversion, a volume representing the whole box was discretized into  $33 \times 33 \times 17$  voxels. The  $\hat{\mu}_{ax}$  computation used  $\sigma = 0.015 \text{ cm}^{-1}$  and  $p = 2$ , and the  $\hat{\mu}_{am}$  computation used  $\sigma = 0.03 \text{ cm}^{-1}$  and  $p = 2$ . For both images, the ICD algorithm was run for 20 iterations on a 927-MHz Pentium III workstation, taking approximately 10 min. The resulting  $\hat{\mu}_{ax}$  and  $\hat{\mu}_{am}$  images show a heterogeneity with accurate shape, although with artifacts present in the region close to the top plate. In

both images, the sphere's vertical positions are similar, but below the true location by approximately 4 or 5 mm. The similarity of the two reconstructions, despite the fact that they are based on independent data sets, suggests that this error is due to a systematic effect in the reconstruction method. This may be a result of calibration errors, as the assumption of a diffuse, homogeneous medium in the baseline calibrations neglected the presence of the low-scattering glass sphere, the plastic stand used to hold the sphere, and the thin rubber tubes used to pump in the ICG solution. Small errors in the assumed  $D_x$  and  $D_m$  values might also contribute to artifacts in the reconstructions. In addition, placing the sphere close to the detectors may have resulted in modeling errors under the diffusion approximation. In  $\hat{\mu}_{ax}$ , the reconstructed ICG absorption is slightly smaller than the predicted value of  $0.039 \text{ cm}^{-1}$ , which one would expect from the results of Sevick-Muraca *et al.*,<sup>16</sup> after correcting for use of 690-nm, rather than 780-nm, excitation with the above-mentioned 30% factor.<sup>38</sup> The  $\hat{\mu}_{am}$  image has higher contrast than

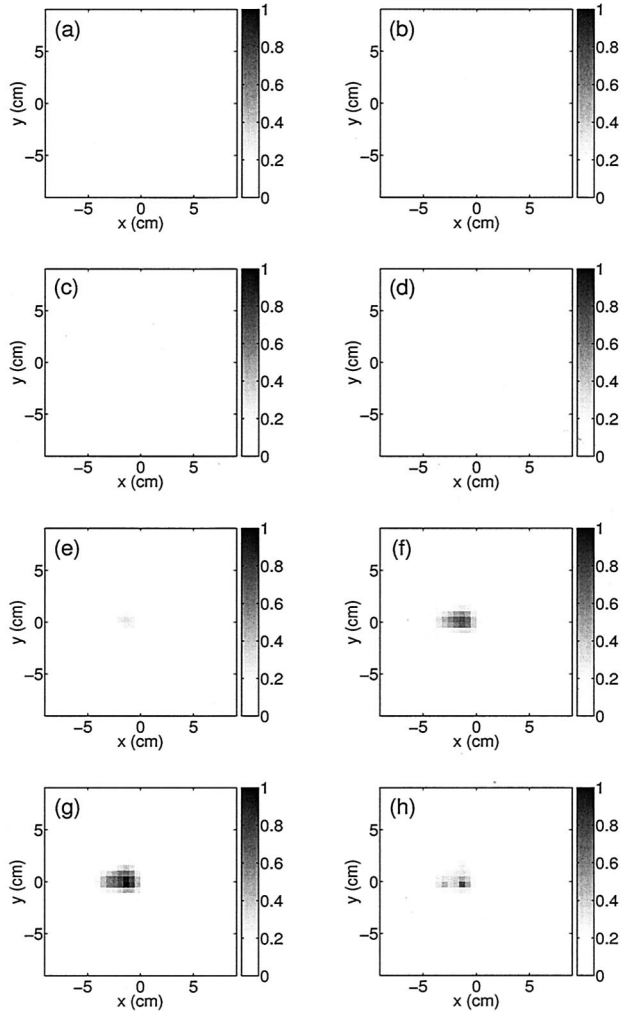


Fig. 13. Reconstructions of  $\eta\mu_{a_f}$  in arbitrary units. Values of  $z$  for (a)–(h) are the same as in Fig. 10.

the  $\hat{\mu}_{a_x}$  image, in contrast to a published absorption spectrum for ICG of  $6.5 \mu\text{mol/l}$ , which shows higher absorption at  $690 \text{ nm}$  than at  $830 \text{ nm}$ . It is possible that ICG's instability in aqueous solution causes some variability in its optical spectrum; Landsman *et al.*<sup>43</sup> observed a shift in the absorption peak toward longer wavelengths with decreasing concentration. In addition, the effect of an Intralipid suspension on ICG's absorption spectrum has not been investigated in detail, to our knowledge.

Figure 13 shows the fluorescent yield reconstruction  $\eta\mu_{a_f}$ . As a result of the unknown scale factor in the fluorescence data, the image is in arbitrary units. Making use of  $\hat{\mu}_{a_x}$  and  $\hat{\mu}_{a_m}$ , we ran the ICD algorithm, using  $p = 2.0$  and  $\sigma = 5.0$  arbitrary units, for 20 iterations (approximately 3 min). The iterations were computationally inexpensive because of the linearity of the fluorescence inverse problem. In contrast to the absorption reconstructions, the reconstructed fluorophore's center is slightly higher than that of the true fluorophore. Although no quantitative information is available, the size and shape are approximately correct.

## 7. Conclusion

We have presented a computationally efficient Bayesian inversion strategy for reconstructing fluorescence, absorption, and scattering properties and demonstrated the method in a simulation study and in a tissue phantom experiment to image fluorescence from ICG in a spherical heterogeneity. The results show potential for use of ODT with fluorescence as a tool for localizing fluorescent contrast agents in clinical diagnostic applications.

It is worth noting that our experimental calibration procedure simplifies the problem substantially because it chooses a background absorption value in advance and observes changes with respect to baseline measurements. We have found that this procedure reconstructs similar-looking absorbers over a wide range of background values. Ongoing research with nonlinear multigrid reconstruction algorithms,<sup>25</sup> automatic source/detector calibration,<sup>29</sup> and more accurate transport models<sup>44</sup> may improve reconstruction accuracy with less favorable calibrations.

Fluorescence imaging may offer some clinical advantages over absorption imaging. One advantage is the possibility of using lifetime as a diagnostic tool. For the yield imaging problem, the error propagation study suggests that qualitative results may be obtainable without one having to perform the full  $\mathbf{x}_x$  and  $\mathbf{x}_m$  inversions. Although the reconstructed lifetime was highly sensitive to incorrect background properties, the reconstructed yield was not. Hence, as Ntziachristos and Weissleder<sup>22</sup> have observed, simplified first-order models are more easily applied to the fluorescent yield imaging problem than to the full absorption imaging problem. This enables a simpler experimental approach that requires no baseline data. For qualitative localization of tumors, this could prove to be a decisive advantage of fluorescence imaging over absorption imaging.

## Appendix A: Fréchet Derivatives

Here we describe the computation of the Fréchet derivatives of the forward operators used in this study. Let  $g(\mathbf{r}_{\text{src}}, \mathbf{r}_{\text{obs}}; \mathbf{x})$  be the diffusion equation Green's function for the problem domain computed with the image vector  $\mathbf{x}$  and a numerical forward solver, with  $\mathbf{r}_{\text{src}}$  as the source location and  $\mathbf{r}_{\text{obs}}$  as the observation point. In addition, suppose that for a particular image  $\mathbf{x}$  there are  $K$  sources and  $M$  detectors and a total of  $P = KM$  measurements. Let  $\mathbf{r}_{s_k}$  represent the position of the  $k$ th source and let  $\mathbf{r}_{d_m}$  represent the position of the  $\{m\}$ th detector. (Here we use the letter  $m$  to denote detector number, as in our previous publications,<sup>24–26,29</sup> but with a prime mark to avoid confusion with the fluorescence emission subscript.) It follows that the computed data vector  $\mathbf{f}(\mathbf{x})$  is given by

$$\mathbf{f}(\mathbf{x}) = [g(\mathbf{r}_{s_1}, \mathbf{r}_{d_1}; \mathbf{x}) \quad g(\mathbf{r}_{s_1}, \mathbf{r}_{d_2}; \mathbf{x}) \quad \cdots \quad g(\mathbf{r}_{s_1}, \mathbf{r}_{d_M}; \mathbf{x}) \\ g(\mathbf{r}_{s_2}, \mathbf{r}_{d_1}; \mathbf{x}) \quad \cdots \quad g(\mathbf{r}_{s_K}, \mathbf{r}_{d_M}; \mathbf{x})]^T. \quad (\text{A1})$$

For image vectors  $\mathbf{x}$  of size  $2N$ , the Fréchet derivative is the  $P \times 2N$  complex matrix given by

$$\mathbf{F}'(\mathbf{x}) = \begin{bmatrix} \frac{\partial g(\mathbf{r}_{s_1}, \mathbf{r}_{d_1}; \mathbf{x})}{\partial x_1} & \frac{\partial g(\mathbf{r}_{s_1}, \mathbf{r}_{d_1}; \mathbf{x})}{\partial x_2} & \dots & \frac{\partial g(\mathbf{r}_{s_1}, \mathbf{r}_{d_1}; \mathbf{x})}{\partial x_{2N-1}} & \frac{\partial g(\mathbf{r}_{s_1}, \mathbf{r}_{d_1}; \mathbf{x})}{\partial x_{2N}} \\ \frac{\partial g(\mathbf{r}_{s_1}, \mathbf{r}_{d_2}; \mathbf{x})}{\partial x_1} & \frac{\partial g(\mathbf{r}_{s_1}, \mathbf{r}_{d_2}; \mathbf{x})}{\partial x_2} & \dots & \frac{\partial g(\mathbf{r}_{s_1}, \mathbf{r}_{d_2}; \mathbf{x})}{\partial x_{2N-1}} & \frac{\partial g(\mathbf{r}_{s_1}, \mathbf{r}_{d_2}; \mathbf{x})}{\partial x_{2N}} \\ \vdots & \vdots & \ddots & \vdots & \vdots \\ \frac{\partial g(\mathbf{r}_{s_1}, \mathbf{r}_{d_M}; \mathbf{x})}{\partial x_1} & \frac{\partial g(\mathbf{r}_{s_1}, \mathbf{r}_{d_M}; \mathbf{x})}{\partial x_2} & \dots & \frac{\partial g(\mathbf{r}_{s_1}, \mathbf{r}_{d_M}; \mathbf{x})}{\partial x_{2N-1}} & \frac{\partial g(\mathbf{r}_{s_1}, \mathbf{r}_{d_M}; \mathbf{x})}{\partial x_{2N}} \\ \frac{\partial g(\mathbf{r}_{s_2}, \mathbf{r}_{d_1}; \mathbf{x})}{\partial x_1} & \frac{\partial g(\mathbf{r}_{s_2}, \mathbf{r}_{d_1}; \mathbf{x})}{\partial x_2} & \dots & \frac{\partial g(\mathbf{r}_{s_2}, \mathbf{r}_{d_1}; \mathbf{x})}{\partial x_{2N-1}} & \frac{\partial g(\mathbf{r}_{s_2}, \mathbf{r}_{d_1}; \mathbf{x})}{\partial x_{2N}} \\ \vdots & \vdots & \ddots & \vdots & \vdots \\ \frac{\partial g(\mathbf{r}_{s_K}, \mathbf{r}_{d_M}; \mathbf{x})}{\partial x_1} & \frac{\partial g(\mathbf{r}_{s_K}, \mathbf{r}_{d_M}; \mathbf{x})}{\partial x_2} & \dots & \frac{\partial g(\mathbf{r}_{s_K}, \mathbf{r}_{d_M}; \mathbf{x})}{\partial x_{2N-1}} & \frac{\partial g(\mathbf{r}_{s_K}, \mathbf{r}_{d_M}; \mathbf{x})}{\partial x_{2N}} \end{bmatrix}. \quad (\text{A2})$$

For the absorption and scattering coefficients, the discrete representations of the Fréchet derivative matrix elements have been derived and reported previously<sup>27,45</sup> as

$$\frac{\partial g(\mathbf{r}_{s_k}, \mathbf{r}_{d_m}; \mathbf{x})}{\partial \mu_a(\mathbf{r}_i)} \approx -g(\mathbf{r}_{d_m}, \mathbf{r}_i; \mathbf{x})g(\mathbf{r}_{s_k}, \mathbf{r}_i; \mathbf{x})V, \quad (\text{A3})$$

$$\frac{\partial g(\mathbf{r}_{s_k}, \mathbf{r}_{d_m}; \mathbf{x})}{\partial D(\mathbf{r}_i)} \approx -\nabla g(\mathbf{r}_{d_m}, \mathbf{r}_i; \mathbf{x}) \cdot \nabla g(\mathbf{r}_{s_k}, \mathbf{r}_i; \mathbf{x})V, \quad (\text{A4})$$

where  $\approx$  is used because of domain discretization errors,  $V$  is the voxel volume,  $\mathbf{r}_i$  is the position of the  $i$ th voxel, and reciprocity<sup>46</sup> [which allows replacement of  $g(\mathbf{r}_{\text{src}}, \mathbf{r}_{\text{obs}}; \mathbf{x})$  with  $g(\mathbf{r}_{\text{obs}}, \mathbf{r}_{\text{src}}; \mathbf{x})$ ] was used to reduce the computation. Here,  $\nabla$  is the spatial gradient operator, which, in our computations, is evaluated numerically as a symmetric first difference. The separability of relations (A3) and (A4) with respect to source index and detector index enables additional savings in computation and in storage.<sup>29</sup> Rather than creating the entire  $KM \times 2N$  matrix, it suffices to initially compute and store two Green's function matrices of sizes  $K \times N$  and  $M \times N$ , respectively:

$$\mathbf{G}^{(s)} = \begin{bmatrix} g(\mathbf{r}_{s_1}, \mathbf{r}_1; \mathbf{x}) & \dots & g(\mathbf{r}_{s_1}, \mathbf{r}_N; \mathbf{x}) \\ \vdots & \ddots & \vdots \\ g(\mathbf{r}_{s_K}, \mathbf{r}_1; \mathbf{x}) & \dots & g(\mathbf{r}_{s_K}, \mathbf{r}_N; \mathbf{x}) \end{bmatrix}, \quad (\text{A5})$$

$$\mathbf{G}^{(d)} = \begin{bmatrix} g(\mathbf{r}_{d_1}, \mathbf{r}_1; \mathbf{x}) & \dots & g(\mathbf{r}_{d_1}, \mathbf{r}_N; \mathbf{x}) \\ \vdots & \ddots & \vdots \\ g(\mathbf{r}_{d_M}, \mathbf{r}_1; \mathbf{x}) & \dots & g(\mathbf{r}_{d_M}, \mathbf{r}_N; \mathbf{x}) \end{bmatrix}. \quad (\text{A6})$$

During the ICD scan, when the  $i$ th voxel of  $\mathbf{x}$  is to be modified, the  $i$ th column of  $\mathbf{F}'(\mathbf{x})$  can be formed from Eqs. (A5) and (A6).

For the fluorescence problem, more specific notation is needed. Let  $g_x(\mathbf{r}_{\text{src}}, \mathbf{r}_{\text{obs}}; \mathbf{x}_x)$  denote the  $\lambda_x$  Green's function obtained when we solve Eq. (1) and let  $g_m(\mathbf{r}_{\text{src}}, \mathbf{r}_{\text{obs}}; \mathbf{x}_m)$  denote the  $\lambda_m$  Green's function

obtained when we solve Eq. (3). We denote the Green's function matrices accordingly:

$$\mathbf{G}_x^{(s)} = \begin{bmatrix} g_x(\mathbf{r}_{s_1}, \mathbf{r}_1; \mathbf{x}_x) & \dots & g_x(\mathbf{r}_{s_1}, \mathbf{r}_N; \mathbf{x}_x) \\ \vdots & \ddots & \vdots \\ g_x(\mathbf{r}_{s_K}, \mathbf{r}_1; \mathbf{x}_x) & \dots & g_x(\mathbf{r}_{s_K}, \mathbf{r}_N; \mathbf{x}_x) \end{bmatrix}, \quad (\text{A7})$$

$$\mathbf{G}_x^{(d)} = \begin{bmatrix} g_x(\mathbf{r}_{d_1}, \mathbf{r}_1; \mathbf{x}_x) & \dots & g_x(\mathbf{r}_{d_1}, \mathbf{r}_N; \mathbf{x}_x) \\ \vdots & \ddots & \vdots \\ g_x(\mathbf{r}_{d_M}, \mathbf{r}_1; \mathbf{x}_x) & \dots & g_x(\mathbf{r}_{d_M}, \mathbf{r}_N; \mathbf{x}_x) \end{bmatrix}, \quad (\text{A8})$$

$$\mathbf{G}_m^{(s)} = \begin{bmatrix} g_m(\mathbf{r}_{s_1}, \mathbf{r}_1; \mathbf{x}_m) & \dots & g_m(\mathbf{r}_{s_1}, \mathbf{r}_N; \mathbf{x}_m) \\ \vdots & \ddots & \vdots \\ g_m(\mathbf{r}_{s_K}, \mathbf{r}_1; \mathbf{x}_m) & \dots & g_m(\mathbf{r}_{s_K}, \mathbf{r}_N; \mathbf{x}_m) \end{bmatrix}, \quad (\text{A9})$$

$$\mathbf{G}_m^{(d)} = \begin{bmatrix} g_m(\mathbf{r}_{d_1}, \mathbf{r}_1; \mathbf{x}_m) & \dots & g_m(\mathbf{r}_{d_1}, \mathbf{r}_N; \mathbf{x}_m) \\ \vdots & \ddots & \vdots \\ g_m(\mathbf{r}_{d_M}, \mathbf{r}_1; \mathbf{x}_m) & \dots & g_m(\mathbf{r}_{d_M}, \mathbf{r}_N; \mathbf{x}_m) \end{bmatrix}. \quad (\text{A10})$$

Consider one reparameterization on the right-hand side of Eq. (2):

$$\eta \mu_{a_f}(\mathbf{r}) \frac{1 - j\omega\tau(\mathbf{r})}{1 + [\omega\tau(\mathbf{r})]^2} = \beta_R(\mathbf{r}) - j\beta_I(\mathbf{r}). \quad (\text{A11})$$

It follows immediately that the inverse problem for  $\beta_R$  and  $\beta_I$  is linear. Let  $g_f(\mathbf{r}_{\text{src}}, \mathbf{r}_{\text{obs}}; \mathbf{x}_x, \mathbf{x}_m)$  denote the fluorescence observed at  $\mathbf{r}_{\text{obs}}$  emitted in response to excitation at  $\mathbf{r}_{\text{src}}$ . The Fréchet derivatives for  $\beta_I$  and  $\beta_R$  are given by

$$\frac{\partial g_f(\mathbf{r}_{s_k}, \mathbf{r}_{d_m}; \mathbf{x}_x, \mathbf{x}_m)}{\partial \beta_R(\mathbf{r}_i)} \approx g_m(\mathbf{r}_{d_m}, \mathbf{r}_i; \mathbf{x}_m) \times g_x(\mathbf{r}_{s_k}, \mathbf{r}_i; \mathbf{x}_x)V, \quad (\text{A12})$$

$$\frac{\partial g_f(\mathbf{r}_{s_k}, \mathbf{r}_{d_m}; \mathbf{x}_x, \mathbf{x}_m)}{\partial \beta_I(\mathbf{r}_i)} \approx -jg_m(\mathbf{r}_{d_m}, \mathbf{r}_i; \mathbf{x}_m) \times g_x(\mathbf{r}_{s_k}, \mathbf{r}_i; \mathbf{x}_x)V. \quad (\text{A13})$$

It is possible to solve the fluorescence inverse problem with this parameterization and then convert the result into the physical parameters  $\eta\mu_{a_f}$  and  $\tau$ . However, the computation of  $\tau$  requires a division of  $\beta_I$  by  $\beta_R$ , an operation that could result in large noise artifacts in regions where  $\beta_R$  is small. To circumvent this problem, we use the  $\gamma$  and  $\tau$  parameterization of Eq. (6), permitting us to apply regularization directly to  $\tau$ . In our sequential update scheme,  $\tau$  is assumed constant while updates of  $\gamma$  are performed, and vice versa. As a result, we use the following Fréchet derivative expressions:

$$\frac{\partial g_f(\mathbf{r}_{s_k}, \mathbf{r}_{d_m}; \mathbf{x}_x, \mathbf{x}_m)}{\partial \gamma(\mathbf{r}_i)} \simeq g_m(\mathbf{r}_{d_m}, \mathbf{r}_i; \mathbf{x}_m) g_x(\mathbf{r}_{s_k}, \mathbf{r}_i; \mathbf{x}_x) \times [1 - j\omega \hat{\tau}(\mathbf{r}_i)] V, \quad (\text{A14})$$

$$\frac{\partial g_f(\mathbf{r}_{s_k}, \mathbf{r}_{d_m}; \mathbf{x}_x, \mathbf{x}_m)}{\partial \tau(\mathbf{r}_i)} \simeq -j\omega \hat{\gamma}(\mathbf{r}_i) g_m(\mathbf{r}_{d_m}, \mathbf{r}_i; \mathbf{x}_m) \times g_x(\mathbf{r}_{s_k}, \mathbf{r}_i; \mathbf{x}_x) V. \quad (\text{A15})$$

After the reconstructions of  $\hat{\mathbf{x}}_x$  and  $\hat{\mathbf{x}}_m$  are obtained,  $\mathbf{G}_x(\mathbf{r}_s, \mathbf{r}; \mathbf{x}_x)$  and  $\mathbf{G}_m(\mathbf{r}_d, \mathbf{r}; \mathbf{x}_m)$  have already been stored, and the Green's functions of relations (A14) and (A15) need not be recomputed. As the estimates  $\hat{\gamma}$  and  $\hat{\tau}$  are updated, they are incorporated into the derivative expressions.

#### Appendix B: Pseudocode for the Inversion Algorithm

```

main {
  1. Initialize  $\hat{\mathbf{x}}_x$ ,  $\hat{\mathbf{x}}_m$ , and  $\hat{\mathbf{x}}_f$  with background estimates.
  2. Repeat until converged: {
    (a)  $\hat{\alpha}_x \leftarrow (1/P_x) \|\mathbf{y}_x - \mathbf{f}_x(\hat{\mathbf{x}}_x)\|_{\Lambda_x}^2$ 
    (b) For  $k = 1:K$  {
      Compute  $g_x(\mathbf{r}_{s_k}, \mathbf{r}; \hat{\mathbf{x}}_x)$  by solving Eq. (1) with source at  $\mathbf{r}_{s_k}$ 
    }
    (c) For  $m' = 1:M$  {
      Compute  $g_x(\mathbf{r}_{d_{m'}}, \mathbf{r}; \hat{\mathbf{x}}_x)$  by solving Eq. (1) with source at  $\mathbf{r}_{d_{m'}}$ 
    }
    (d) Form  $\mathbf{G}_x^{(s)}$  and  $\mathbf{G}_x^{(d)}$  with Eqs. (A7) and (A8)
    (e)  $\hat{\mathbf{x}}_x \leftarrow \text{ICD\_update}[\hat{\mathbf{x}}_x, \hat{\alpha}_x, \mathbf{G}_x^{(s)}, \mathbf{G}_x^{(d)}]$ 
  }
  3. Repeat until converged: {
    (a)  $\hat{\alpha}_m \leftarrow 1/P_m \|\mathbf{y}_m - \mathbf{f}_m(\hat{\mathbf{x}}_m)\|_{\Lambda_m}^2$ 
    (b) For  $k = 1:K$  {
      Compute  $g_m(\mathbf{r}_{s_k}, \mathbf{r}; \hat{\mathbf{x}}_m)$  by solving Eq. (3) with source at  $\mathbf{r}_{s_k}$ 
    }
    (c) For  $m' = 1:M$  {
      Compute  $g_m(\mathbf{r}_{d_{m'}}, \mathbf{r}; \hat{\mathbf{x}}_m)$  by solving Eq. (3) with source at  $\mathbf{r}_{d_{m'}}$ 
    }
    (d) Form  $\mathbf{G}_m^{(s)}$  and  $\mathbf{G}_m^{(d)}$  with Eqs. (A9) and (A10)
    (e)  $\hat{\mathbf{x}}_m \leftarrow \text{ICD\_update}[\hat{\mathbf{x}}_m, \hat{\alpha}_m, \mathbf{G}_m^{(s)}, \mathbf{G}_m^{(d)}]$ 
  }
  4. Repeat until converged: {
    (a)  $\hat{\alpha}_f \leftarrow (1/P_f) \|\mathbf{y}_f - \mathbf{f}_f(\hat{\mathbf{x}}_f, \hat{\mathbf{x}}_x, \hat{\mathbf{x}}_m)\|_{\Lambda_f}^2$ 

```

```

    (b)  $\hat{\mathbf{x}}_f \leftarrow \text{ICD\_update}[\hat{\mathbf{x}}_f, \hat{\alpha}_f, \mathbf{G}_x^{(s)}, \mathbf{G}_m^{(d)}]$ 
  }
}

 $\hat{\mathbf{x}} \leftarrow \text{ICD\_update}[\hat{\mathbf{x}}, \hat{\alpha}, \mathbf{G}^{(s)}, \mathbf{G}^{(d)}; \mathbf{x}]$  {
  1. For  $i = 1, \dots, N$  (in random order), {
    (a) Compute  $[\mathbf{F}'(\hat{\mathbf{x}})]_{*(i)}$ , as described in Appendix A
    (b) Update  $x_i$ , as described by Ye et al.24:


$$\hat{x}_i \leftarrow \arg \min_{x_i \geq 0} \left\{ \frac{1}{\hat{\alpha}} \|\mathbf{y} - \mathbf{f}(\hat{\mathbf{x}}) - [\mathbf{F}'(\hat{\mathbf{x}})]_{*(i)}(x_i - \hat{x}_i)\|_{\Lambda}^2 + \frac{1}{p_a \sigma_a^{p_a}} \sum_{j \in N_i} b_{i-j} |x_i - \hat{x}_i|^{p_a} \right\}$$

  }
  2. For  $i = N + 1, \dots, 2N$  (in random order), {
    (a) Compute  $[\mathbf{F}'(\hat{\mathbf{x}})]_{*(i)}$ , as described in Appendix A
    (b) Update  $x_i$ , as described by Ye et al.24:


$$\hat{x}_i \leftarrow \arg \min_{x_i \geq 0} \left\{ \frac{1}{\hat{\alpha}} \|\mathbf{y} - \mathbf{f}(\hat{\mathbf{x}}) - [\mathbf{F}'(\hat{\mathbf{x}})]_{*(i)}(x_i - \hat{x}_i)\|_{\Lambda}^2 + \frac{1}{p_b \sigma_b^{p_b}} \sum_{j \in N_i} b_{i-j} |x_i - \hat{x}_i|^{p_b} \right\}$$

  }
  3. Return  $\hat{\mathbf{x}}$ .
}

```

This research was funded by the National Science Foundation under contract CCR-0073357. Quan Zhang and David A. Boas acknowledge support from Advanced Research Technologies Inc. In addition, we thank Tina Chaves for her assistance with the laboratory equipment.

#### References

1. S. R. Arridge, "Optical tomography in medical imaging," *Inverse Probl.* **15**, R41–R93 (1999).
2. D. A. Boas, D. H. Brooks, E. L. Miller, C. A. DiMarzio, M. Kilmer, R. J. Gaudette, and Q. Zhang, "Imaging the body with diffuse optical tomography," *IEEE Signal Process. Mag.* **18**, 57–75 (2001).
3. V. G. Peters, D. R. Wyman, M. S. Patterson, and G. L. Frank, "Optical properties of normal and diseased human breast tissues in the visible and near infrared," *Phys. Med. Biol.* **35**, 1317–1334 (1990).
4. T. L. Troy, D. L. Page, and E. M. Sevick-Muraca, "Optical properties of normal and diseased breast tissue: prognosis for optical mammography," *J. Biomed. Opt.* **1**, 342–355 (1996).
5. A. Pèlerin, S. Folli, F. Buchegger, J. Mach, G. Wagnières, and H. van den Bergh, "Antibody-fluorescein conjugates for photoimmunodiagnosis of human colon carcinoma in nude mice," *Cancer* **67**, 2529–2537 (1991).
6. B. Ballou, G. W. Fisher, T. R. Hakala, and D. L. Farkas, "Tumor detection and visualization using cyanine fluorochrome-labeled antibodies," *Biotechnol. Prog.* **13**, 649–658 (1997).

7. R. Cubeddu, G. Canti, A. Pifferi, P. Taroni, and G. Valentini, "Fluorescence lifetime imaging of experimental tumors in hematoporphyrin derivative-sensitized mice," *Photochem. Photobiol.* **66**, 229–236 (1997).
8. J. A. Reddy and P. S. Low, "Folate-mediated targeting of therapeutic and imaging agents to cancers," *Crit. Rev. Ther. Drug Carrier Syst.* **15**, 587–627 (1998).
9. J. S. Reynolds, T. L. Troy, R. H. Mayer, A. B. Thompson, D. J. Waters, K. K. Cornell, P. W. Snyder, and E. M. Sevick-Muraca, "Imaging of spontaneous canine mammary tumors using fluorescent contrast agents," *Photochem. Photobiol.* **70**, 87–94 (1999).
10. U. Mahmood, C. Tung, J. A. Bogdanov, and R. Weissleder, "Near-infrared optical imaging of protease activity for tumor detection," *Radiology* **213**, 866–870 (1999).
11. K. Licha, B. Riefke, V. Ntziachristos, A. Becker, B. Chance, and W. Semmler, "Hydrophilic cyanine dyes as contrast agents for near-infrared tumor imaging: synthesis, photophysical properties and spectroscopic *in vivo* characterization," *Photochem. Photobiol.* **72**, 392–398 (2000).
12. V. Ntziachristos, A. G. Yodh, M. Schnall, and B. Chance, "Concurrent MRI and diffuse optical tomography of breast after indocyanine green enhancement," *Proc. Natl. Acad. Sci. USA* **97**, 2767–2772 (2000).
13. A. Becker, C. Hessesen, K. Licha, B. Ebert, U. Sukowski, W. Semmler, B. Wiedenmann, and C. Grotzinger, "Receptor-targeted optical imaging of tumors with near-infrared fluorescent ligands," *Nat. Biotechnol.* **19**, 327–331 (2001).
14. J. E. Bugaj, S. Achilefu, R. B. Dorshow, and R. Rajagopalan, "Novel fluorescent contrast agents for optical imaging of *in vivo* tumors based on a receptor-targeted dye-peptide conjugate platform," *J. Biomed. Opt.* **6**, 122–133 (2001).
15. M. S. Patterson and B. W. Pogue, "Mathematical model for time-resolved and frequency-domain fluorescence spectroscopy in biological tissues," *Appl. Opt.* **33**, 1963–1974 (1994).
16. E. M. Sevick-Muraca, G. Lopez, J. S. Reynolds, T. L. Troy, and C. L. Hutchinson, "Fluorescence and absorption contrast mechanisms for biomedical optical imaging using frequency-domain techniques," *Photochem. Photobiol.* **66**, 55–64 (1997).
17. R. Roy and E. M. Sevick-Muraca, "Three-dimensional unconstrained and constrained image-reconstruction techniques applied to fluorescence, frequency-domain photon migration," *Appl. Opt.* **40**, 2206–2215 (2001).
18. M. A. O'Leary, D. A. Boas, X. D. Li, B. Chance, and A. G. Yodh, "Fluorescence lifetime imaging in turbid media," *Opt. Lett.* **21**, 158–160 (1996).
19. D. Paithankar, A. Chen, B. Pogue, M. Patterson, and E. Sevick-Muraca, "Imaging of fluorescent yield and lifetime from multiply scattered light reemitted from random media," *Appl. Opt.* **36**, 2260–2272 (1997).
20. H. Jiang, "Frequency-domain fluorescent diffusion tomography: a finite-element-based algorithm and simulations," *Appl. Opt.* **37**, 5337–5343 (1998).
21. J. Chang, H. L. Graber, and R. L. Barbour, "Luminescence optical tomography of dense scattering media," *J. Opt. Soc. Am. A* **14**, 288–299 (1997).
22. V. Ntziachristos and R. Weissleder, "Experimental three-dimensional fluorescence reconstruction of diffuse media by use of a normalized Born approximation," *Opt. Lett.* **26**, 893–895 (2001).
23. D. A. Boas, "A fundamental limitation of linearized algorithms for diffuse optical tomography," *Opt. Express* **1**, 404–413 (1997); <http://www.opticsexpress.org>.
24. J. C. Ye, K. J. Webb, C. A. Bouman, and R. P. Millane, "Optical diffusion tomography by iterative-coordinate-descent optimization in a Bayesian framework," *J. Opt. Soc. Am. A* **16**, 2400–2412 (1999).
25. J. C. Ye, C. A. Bouman, K. J. Webb, and R. P. Millane, "Nonlinear multigrid algorithms for Bayesian optical diffusion tomography," *IEEE Trans. Image Process.* **10**, 909–922 (2001).
26. A. B. Milstein, S. Oh, J. S. Reynolds, K. J. Webb, C. A. Bouman, and R. P. Millane, "Three-dimensional Bayesian optical diffusion tomography with experimental data," *Opt. Lett.* **27**, 95–97 (2002).
27. J. C. Ye, K. J. Webb, R. P. Millane, and T. J. Downar, "Modified distorted Born iterative method with an approximate Fréchet derivative for optical diffusion tomography," *J. Opt. Soc. Am. A* **16**, 1814–1826 (1999).
28. J. S. Reynolds, C. A. Thompson, K. J. Webb, F. P. LaPlant, and D. Ben-Amotz, "Frequency domain modeling of reradiation in highly scattering media," *Appl. Opt.* **36**, 2252–2259 (1997).
29. S. Oh, A. B. Milstein, R. P. Millane, C. A. Bouman, and K. J. Webb, "Source-detector calibration in three-dimensional Bayesian optical diffusion tomography," *J. Opt. Soc. Am. A* **19**, 1983–1993 (2002).
30. C. A. Bouman and K. Sauer, "A generalized Gaussian image model for edge-preserving MAP estimation," *IEEE Trans. Image Process.* **2**, 296–310 (1993).
31. K. Sauer and C. A. Bouman, "A local update strategy for iterative reconstruction from projections," *IEEE Trans. Signal Process.* **41**, 534–548 (1993).
32. J. C. Adams, "MUDPACK: multigrid portable FORTRAN software for the efficient solution of linear elliptic partial differential equations," *Appl. Math. Comput.* **34**, 113–146 (1989).
33. J. J. Duderstadt and L. J. Hamilton, *Nuclear Reactor Analysis* (Wiley, New York, 1976).
34. S. S. Saquib, C. A. Bouman, and K. Sauer, "ML parameter estimation for Markov random fields with applications to Bayesian tomography," *IEEE Trans. Image Process.* **7**, 1029–1044 (1998).
35. S. Oh, A. B. Milstein, C. A. Bouman, and K. J. Webb, "Multigrid inversion algorithms with applications to optical diffusion tomography," in *Proceedings of the 36th Asilomar Conference on Signals, Systems, and Computers* (Institute of Electrical and Electronics Engineers, New York, 2002), pp. 901–905.
36. K. Sauer and C. Bouman, "Bayesian estimation of transmission tomograms using segmentation based optimization," *IEEE Trans. Nucl. Sci.* **39**, 1144–1152 (1992).
37. Q. Zhang, T. J. Brukilacchio, T. Gaudett, L. Wang, A. Li, and D. A. Boas, "Experimental comparison of using continuous-wave and frequency-domain diffuse optical imaging systems to detect heterogeneities," in *Optical Tomography and Spectroscopy of Tissue IV*, B. Chance, R. R. Alfano, B. J. Tromberg, M. Tamura, and E. M. Sevick-Muraca, eds., *Proc. SPIE* **4250**, 219–238 (2001).
38. R. H. Mayer, J. S. Reynolds, and E. M. Sevick-Muraca, "Measurement of the fluorescence lifetime in scattering media by frequency-domain photon migration," *Appl. Opt.* **38**, 4930–4938 (1999).
39. H. J. van Staveren, C. J. M. Moes, J. van Marie, S. A. Prahl, and M. J. C. van Gemert, "Light scattering in Intralipid-10% in the wavelength range of 400–1100 nm," *Appl. Opt.* **30**, 4507–4514 (1991).
40. G. M. Hale and M. R. Querry, "Optical constants of water in the 200-nm to 200- $\mu$ m wavelength region," *Appl. Opt.* **12**, 555–563 (1973).
41. R. C. Benson and H. A. Kues, "Fluorescence properties of indocyanine green as related to angiography," *Phys. Med. Biol.* **23**, 159–163 (1978).
42. D. Boas, T. Gaudette, and S. Arridge, "Simultaneous imaging and optode calibration with diffuse optical tomography," *Opt. Exp.* **8**, 263–270 (2001); <http://opticsexpress.org>.
43. M. L. J. Landsman, G. Kwant, G. A. Mook, and W. G. Zijlstra,

- “Light-absorbing properties, stability, and spectral stabilization of indocyanine green,” *J. Appl. Physiol.* **40**, 575–583 (1976).
44. A. D. Klose and A. H. Hielscher, “A transport-theory-based reconstruction algorithm for optical tomography,” in *Optical Tomography and Spectroscopy of Tissue III*, B. Chance, R. R. Alfano, and B. J. Tromberg, eds., Proc. SPIE **3597**, 26–35 (1999).
45. S. R. Arridge, “Photon-measurement density functions. Part 1: Analytical forms,” *Appl. Opt.* **34**, 7395–7409 (1995).
46. W. C. Chew, *Waves and Fields in Inhomogeneous Media* (Van Nostrand Reinhold, New York, 1990).